RSC Advances

ROYAL SOCIETY OF CHEMISTRY

www.rsc.org/advances

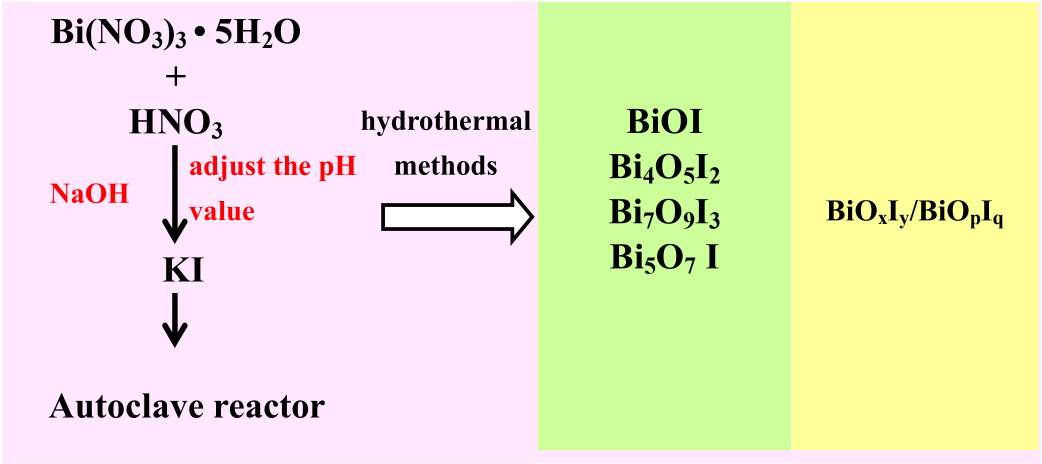

Figure abstract. Schematic diagram of synthesis method for as-prepared BiO_xI_y/BiO_pI_q under different conditions.

RSC Advances RSCPublishing

PAPER

Cite this: DOI: 10.1039/x0xx00000x
Received 00th January 2012,
Accepted 00th January 2012
DOI: 10.1039/x0xx00000x
www.rsc.org/

Synthesis of Bismuth Oxyiodides and Their Composites: Characterization, Photocatalytic Activity, and Degraded Mechanisms

Wenlian William Lee, [b,c,]* Chung-Shin Lu, [d] Chung-Wei Chuang, [a] Yen-Ju Chen, [a] Jing-Ya Fu, [a] Ciao-Wei Siao, [a] Chiing-Chang Chen [a,]*

Bismuth oxyiodides have been prepared using controlled hydrothermal methods. The products are characterized by SEM-EDS, XRD, XPS, FTIR, PL, EPR, and DRS. It is illustrated that BiOI, $Bi_4O_5I_2$, $Bi_7O_9I_3$, Bi_5O_7I, and BiO_xI_y/BiO_pI_q composites can be selectively synthesized through a facile solution-based hydrothermal method. UV-Vis spectra display the bismuth oxyiodide materials as indirect semiconductors with an optical bandgap of 1.86-3.316 eV. The photocatalytic efficiency of the powder suspension is evaluated by measuring the Crystal Violet (CV) concentration. This is the first study to demonstrate the superior activities of BiOI, $Bi_4O_5I_2$, $Bi_7O_9I_3$, Bi_5O_7I, and BiO_xI_y/BiO_pI_q composites as promising visible-light-responsive photocatalysts. The quenching effects of various scavengers and EPR indicate that the reactive $O_2^{\bullet-}$ plays a major role and $^{\bullet}OH$ and h^+ play a minor role. The $Bi_7O_9I_3/Bi_5O_7I$ composite shows the highest photocatalytic activity reaching the maximum rate constant of 0.2225 h^{-1}, which is 6 times higher than that of BiOI and $Bi_7O_9I_3$ and 4 times higher than that of Bi_5O_7I.

1. Introduction

As current energy and environmental problems are the two most important topics in human life, a novel approach to overcome these problems is an imperative affair. Heterogeneous photocatalysis for solar energy conversion and environmental remediation has fomented extensive interests in the past decade. For the practical applications of photocatalysis, an environmentally powerful and cheap photocatalyst is an important constituent. [1] Among various photocatalytic materials, TiO_2 is researched the most; however, it can only be activated by UV light irradiation, which contains less than 5% of the solar spectrum.[2] Accordingly, preparing novel visible-light-responsive photocatalysts [3,4] and searching their photocatalysis activities are of great interests and potential rewards.[5]

Recently, the development of visible-light-sensitive photocatalysts has received considerable attention as an alternative of wastewater treatment. An effective and simple strategy to improve the photocatalytic activity of a photocatalyst is the incorporation of a heterostructure (or composites), because heterojunctions (or composites) have great potential for tuning the desired electronic properties of composite photocatalysts and efficiently separating the photogenerated electron–hole pairs.[6-14]

In recent years, as a new family of advantageous photocatalysts, the bismuth oxyhalides (BiOX, X = Cl, Br, and I) [15,16] have showed unusual photocatalytic activities because their uniquely layered structure features an internal static electric field vertical to each layer that may cause more effective separation of photogenerated charge carriers. It is found that the BiOI sample shows higher photocatalytic activities than BiOBr and BiOCl materials do for the photocatalytic degradation of methyl orange organic pollutants. Among the bismuth oxyhalides,[17] bismuth oxyiodides have obtained remarkable interests in recent years because of their suitable band gaps, stability, and relatively superior photocatalytic activites.[18-20]

The Xiao group synthesized BiOI by ethanol–water mixed solvent methods, which demonstrated excellent photocatalytic abilities and good stability during the phenol photodegradation under visible-light irradiation.[16] Lei et al. showed the synthesis of flower-like BiOI structures by a solution route at room temperature, and the BiOI construction showed higher photocatalytic efficiency toward Methylene Blue, Methyl Orange, and Rhodamine B under visible-light irradiation.[21] BiOI had the small band gap and a strong absorption in the visible light region, and thus showed excellent photocatalytic activities under sun-light irradiation.[22] Aside from BiOI (Bi:I = 1:1 or O:I = 1:1), other I-poor bismuth oxyiodides, including $Bi_4O_5I_2$,[23] $Bi_7O_9I_3$,[24] and Bi_5O_7I,[25,26] were also described. Since the valence band for bismuth oxyiodides mostly contained I 5p and O 2p orbitals, while the conduction band was based on the Bi 6p orbital,[27] it could be demonstrated that the I-poor bismuth oxyiodides had the band-gap energy higher than BiOI but lower than Bi_2O_3;[28,29] hence, these materials might be used as visible-light responsive photocatalysts. More importantly, the structure and composition of the bismuth oxyiodides strongly influenced their electronic, optical, and oxidizing abilities and other physicochemical properties, proposing an opportunity to acquire novel photocatalysts for effective degradation of environmental and toxic pollutants. However, the synthesis methods, characterization, and evaluated properties of a series bismuth oxyiodides remained rare until recently.

Recently, $Bi_xO_yBr_z$,[30] BiOI/ZnO,[31] $BiOI/TiO_2$,[32] BiOI/g-C_3N_4,[33] $BiOI/BiPO_4$,[34] and BiOI/graphene[35] composites have been synthesized in order to improve the photocatalytic activity of the materials. It is well-known that porous and hollow solids have excellent adsorptive properties that possess numerous applications in catalysis. Regardless of these advances, the differences in desired geometry for bismuth oxyiodide porous and hollow shape materials with high photocatalytic efficiency remain to be searched to meet the ever-increasing demand.

Cationic triarylmethane dyes were found the use as colorants in industry and as antimicrobial agents.[36] Recent reports showed that they might further supply as targetable sensitizers in the photo-destruction of specific cellular components (or cells).[37] The binding of CV to DNA was probably ionic, as opposed to intercalative, and it persisted so stably bound to double-stranded DNA that, with its conversion to the colorless carbinol form, it was used for assessing the binding of other molecules to DNA.[38] However, great troubles were arisen about the thyroid peroxidase-catalyzed oxidation of the triarylmethane class of dyes because the reactions might produce various N-de-alkylated primary and secondary aromatic amines, with the structures similar to aromatic amine carcinogens.[39]

CV dye degradations were studied using several systems that generated active species, including $Bi_xAg_yO_z$,[40] Bi2WO6,[41] TiO_2,[42] ZnO,[43] BiOCl/BiOBr,[44] and $BaTiO_3$.[45] In most cases, the reaction mechanisms, kinetics, and efficiency were well known. However, the efficiencies, mechanisms of the BiO_xI_y/BiO_pI_q-assisted photocatalytic degradation of triarylmethane dye under visible light irradiation have never been reported.

To the best of our knowledge, the photocatalytic degradation of organic pollutants by BiO_xI_y/BiO_pI_q has not been published in the literature. These studies synthesize BiOI, $Bi_4O_5I_2$, $Bi_7O_9I_3$, Bi_5O_7I, and BiO_xI_y/BiO_pI_q composites and research their photocatalytic activities for degrading CV in aqueous solutions under visible-light irradiation.

2. Experiment

2.1 Materials

The CV dye (TCI), Bi $(NO_3)_3$•$5H_2O$, p-benzoquinone (Alfa Assar), sodium azide (Sigma), ammonium oxalate (Osaka), isopropanol (Merck) and KI (Katayama) were obtained and used without any further purification. 5,5-Dimethyl-1-pyrroline N-oxide (DMPO) was purchased from Sigma-Aldrich. Reagent-grade NaOH, HNO_3, CH_3COONH_4, and HPLC-grade methanol were purchased from Merck. The de-ionized water used in this research was purified with a Milli-Q water ion-exchange system for a resistivity of 1.80×107 Ω-cm.

Table 1. Codes of bismuth oxyiodide prepared under different hydrothermal conditions. ($Bi(NO_3)_3$/KI = 5/2, pH = 1-14, temp = 130-280 °C, time = 12h)

pH value	Temperature(°C)			
	130	180	230	280
1	B5I2-1-130	B5I2-1-180	B5I2-1-230	B5I2-1-280
2	B5I2-2-130	B5I2-2-180	B5I2-2-230	B5I2-2-280
3	B5I2-3-130	B5I2-3-180	B5I2-3-230	B5I2-3-280
4	B5I2-4-130	B5I2-4-180	B5I2-4-230	B5I2-4-280
5	B5I2-5-130	B5I2-5-180	B5I2-5-230	B5I2-5-280
6	B5I2-6-130	B5I2-6-180	B5I2-6-230	B5I2-6-280
7	B5I2-7-130	B5I2-7-180	B5I2-7-230	B5I2-7-280
8	B5I2-8-130	B5I2-8-180	B5I2-8-230	B5I2-8-280
9	B5I2-9-130	B5I2-9-180	B5I2-9-230	B5I2-9-280
10	B5I2-10-130	B5I2-10-180	B5I2-10-230	B5I2-10-280
11	B5I2-11-130	B5I2-11-180	B5I2-11-230	B5I2-11-280
12	B5I2-12-130	B5I2-12-180	B5I2-12-230	B5I2-12-280
13	B5I2-13-130	B5I2-13-180	B5I2-13-230	B5I2-13-280
14	B5I2-14-130	B5I2-14-180	B5I2-14-230	B5I2-14-280

Table 2. Codes of bismuth oxyiodide prepared under different hydrothermal conditions. ($Bi(NO_3)_3$/KI = 5/25-5/1, pH = 1-14, temp = 280 °C, time = 12h)

Bi/I Molar ratio	pH					
	1	4	7	10	13	14
5:1	B5I1-1-280	B5I1-4-280	B5I1-7-280	B5I1-10-280	B5I1-13-280	B5I1-14-280
5:2	B5I2-1-280	B5I2-4-280	B5I2-7-280	B5I2-10-280	B5I2-13-280	B5I2-14-280
5:5	B5I5-1-280	B5I5-4-280	B5I5-7-280	B5I5-10-280	B5I5-13-280	B5I5-14-280
5:10	B5I10-1-280	B5I10-4-280	B5I10-7-280	B5I10-10-280	B5I10-13-280	B5I10-14-280
5:25	B5I25-1-280	B5I25-4-280	B5I25-7-280	B5I25-10-280	B5I25-13-280	B5I25-14-280

2.2 Synthesis of bismuth oxyiodide

5 mmol Bi $(NO_3)_3$•$5H_2O$ and 5 mL of 4M HNO_3 were added in a 100 mL flask. With continuous stirring, 2 M NaOH was added dropwise to adjust the pH value to 1–14, and then, when a white precipitate was formed, 2 mL of 3 M KI was also added dropwise. The solution was then stirred continuously for 30 min and delivered into a 30 mL Teflon-lined autoclave, which was heated to 130–280 ^{o}C for 12 h and then naturally cooled to room temperature. The resulting precipitate was collected by filtration, washed with deionized water and acetone to remove any possible ionic-species in the precipitate, and then dried at 60 ^{o}C overnight. Depending on the Bi $(NO_3)_3$•$5H_2O$/KI molar ratio (Bi/I = 5/1,5/2, 5/5, 5/10, 5/25), pH value, and reaction temperature, the BiOxIy/BiOpIq composites were prepared and marked as shown in **Tables 1-2**; the as-prepared samples were named from B5I2-1-130 to B5I25-14-280.

2.3 Characterization

The products were further characterized. XRD was measured on a MAC Science, MXP18 X-ray diffractometer with Cu Kα radiation, and operated at 40 kV and 80 mA. EPR spectra were detected using a Bruker EMX-10/12 electron paramagnetic resonance spectrometer. FE-SEM-EDS measurements were performed with a field-emission microscope (JEOL JSM-7401F) at an acceleration voltage of 15 kV. HRXPS measurement was conducted with ULVAC-PHI XPS. Cryogenic cathodoluminescence (CL) measurements were obtained using a JEOL JSM7001F microscope. DR UV-vis spectra measurements were conducted using a Shimadzu UV-2100S spectrophotometer. The HPLC-MS system consisted of a Waters 1525 binary pump, a 717 plus autosampler, a 2998 photodiode array detector, and a ZQ2000 micromass detector.

2.4 Photocatalytic reaction

Photocatalytic activities of bismuth oxyiodides were studied by degrading CV under visible-light irradiation of a 150 W Xe arc. The light intensity was fixed on 32.1 W/m_2 when the reactor was placed 30 cm away from the light source. The aqueous suspension of CV (100 mL, 10 ppm) and the given amount of catalysts were placed in a Pyrex flask. The pH value of the suspension was adjusted by adding either NaOH or HNO_3 solution. Before the irradiation, the suspension was magnetically stirred in the dark to approach an adsorption/desorption equilibrium between the dye and the catalyst surface under ambient air-equilibrated conditions. At the given irradiation time intervals, 5 mL of aliquot was collected and centrifuged to withdrew the catalyst. The supernatant was analyzed by HPLC-MS after re-adjusting the chromatographic conditions to make the mobile phase congruous with the working conditions of the mass spectrometer.

3. Results and discussion

3.1 Characterizations of as-prepared powders

3.1.1 XRD analysis

The X-ray diffraction data of the as-prepared bismuth oxyiodide with different hydrothermal parameters are displayed in **Figures 1-2** and Figures S1-S3 (ESI†). **Tables 3-4** list the results of the XRD measurements. The XRD patterns clearly demonstrated the existence of pure phase and the coexistence of different phases. All the bismuth oxyiodide samples using the hydrothermal method described at different molar ratio, reaction temperature, and pH presented the BiOI (JCPDS 73-2062), $Bi_4O_5I_2$,[19] $Bi_7O_9I_3$,[20] and Bi_5O_7I (JCPDS 40-0548), α-Bi_2O_3 (JCPDS 41-1449), and BiO_xI_y/BiO_pI_q composite phase.

The pH of a hydrothermal reaction is usually accepted to have great influence on determining the morphologies and composition of the final products.[21] Controlled experiments

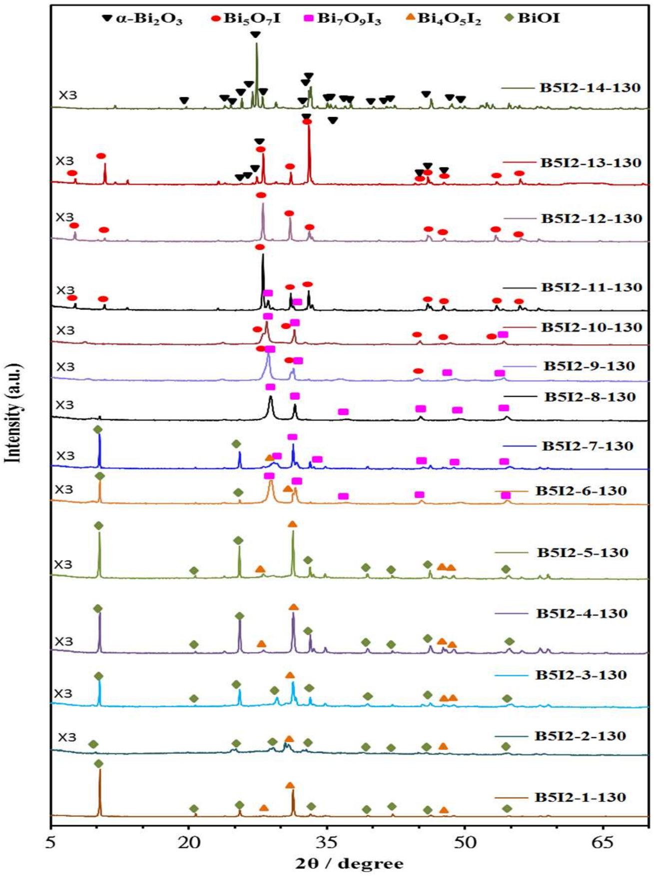

Figure 1. XRD patterns of as-prepared bismuth oxyiodide samples under different pH values, at reaction temperature 130 ^{o}C and reaction times 12 h. (Molar ratio $Bi(NO_3)_3$/KI =5/2)

have been conducted to study the influence of pH on the reaction. In these experiments, pH played a key role, and temperature and molar ratio played a minor role in controlling the composition and anisotropic growth of crystals. From the results summarized in **Table 3**, the controllable morphologies and crystal phases of bismuth oxyiodides could be completed by simply changing some growth parameters, including temperature and pH. BiOI was obtained at pH = 1-7 and temp = 130 °C, pH = 1-6 and temp = 180 °C, pH = 1-5 and temp = 230 °C, and pH = 1-2, temp = 280 °C; $Bi_4O_5I_2$ was obtained at pH = 1-6 and temp = 130 °C, pH = 1-5 and temp = 180-230 °C, and pH = 1-2, temp = 280 °C; $Bi_7O_9I_3$ was obtained at pH = 6-11 and temp = 130-180 °C, pH = 4-11 and temp = 230 °C, and pH = 2-11 and temp = 280 °C; Bi_5O_7I was obtained at pH = 9-13 and temp = 130°C, pH = 8-13 and temp = 180-230°C, and pH = 7-13 and temp = 280°C; and, Bi_2O_3 microstructures were obtained at higher base concentration (pH = 13) in the synthetic conditions. From the results summarized in **Table 4**, the controllable morphologies and crystal phases of bismuth oxyiodides could be completed by simply changing some growth parameters, including pH and molar ratio.

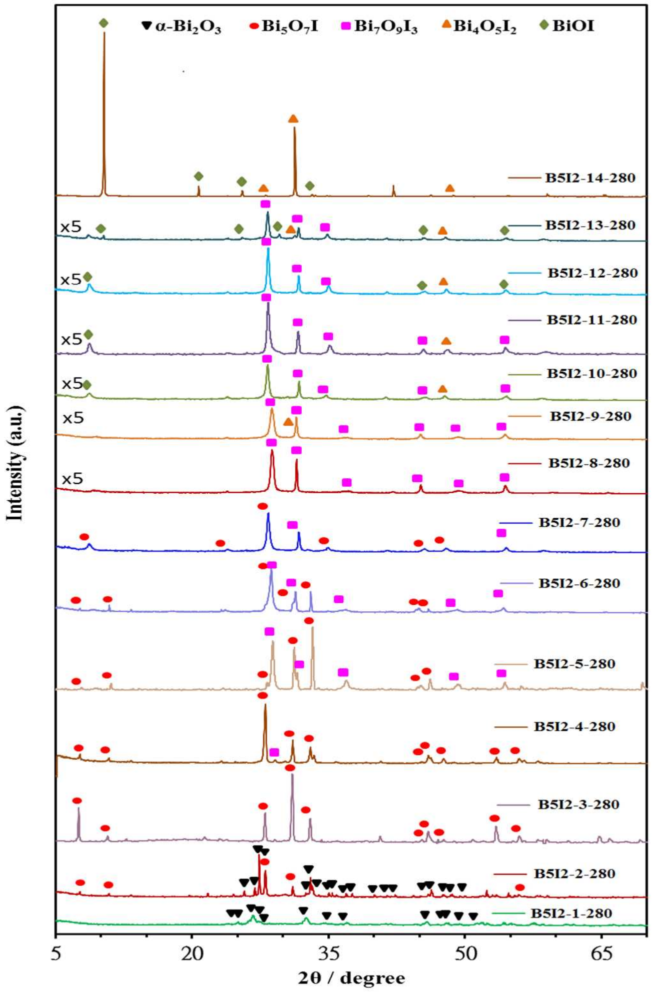

Figure 2. XRD patterns of as-prepared bismuth oxyiodide samples under different pH values, at reaction temperature 280 °C and reaction times 12 h. (Molar ratio $Bi(NO_3)_3$/KI =5/2)

Table 3. Crystalline phase changes of bismuth oxyiodide nanosheets prepared under different reaction conditions. (◆BiOI; ▲$Bi_4O_5I_2$; ■$Bi_7O_9I_3$; ●Bi_5O_7I; ▼α-Bi_2O_3)

pH value	Mole ratio = 5：2 (Bi：I)			
	130	180	230	280
1	◆▲	◆▲	◆▲	◆▲
2	◆▲	◆▲	◆▲	◆▲■
3	◆▲	◆▲	◆▲	■
4	◆▲	◆▲	◆▲■	■
5	◆▲	◆▲	◆▲■	■
6	◆▲■	◆■	■	■
7	◆■	■	■	■●
8	■	■●	■●	■●
9	■●	■●	■●	■●
10	■●	■●	■●	■●
11	■●	■●	■●	■●
12	●	●	●	●
13	●▼	●▼	●▼	●▼
14	▼	▼	▼	▼

BiOI was obtained at pH = 1-7 and molar ratio = 5/25, 5/10, pH = 1-4 and molar ratio = 5/5, and pH = 1 and molar ratio = 5/1, 5/2, and pure phase BiOI at pH = 1 and molar ratio = 5/10, 5/25; $Bi_4O_5I_2$ was obtained at pH = 4-7 and molar ratio = 5/25, 5/10, pH = 1-7 and molar ratio = 5/5, and pH = 1 and molar ratio = 5/1, 5/2; $Bi_7O_9I_3$ was obtained at pH = 7-14 and molar ratio = 5/25, 5/10, pH = 7-13 and molar ratio = 5/5, and pH = 4-10 and molar ratio = 5/2, 5/1; Bi_5O_7I was obtained at pH = 10-14 and molar ratio = 5/25, 5/10, 5/5, pH = 10-13 and molar ratio = 5/2, and pH = 4-13 and molar ratio = 5/1 ; and, Bi_2O_3 microstructures were obtained at higher base concentration (pH = 13-14 and molar ratio = 5/1, 5/2, and pH = 14 and molar ratio = 5/5) in the synthetic conditions.

Table 4. Crystalline phase changes of bismuth oxyiodide prepared under different reaction conditions. (◆ BiOI; ▲ $Bi_4O_5I_2$; ■ $Bi_7O_9I_3$; ● Bi_5O_7I; ▼ α-Bi_2O_3)

pH value	Molar ratio = Bi：I (at 280℃)				
	5：1	5：2	5：5	5：10	5：25
1	◆▲	◆▲	◆▲	◆	◆
4	■●	■	◆▲	◆▲	◆▲
7	■●	■	▲■	◆▲■	◆▲■
10	■●	■●	■●	■●	■●
13	●▼	●▼	■●	■●	■●
14	▼	▼	●▼	■●	■●

The production of bismuth oxyiodides included the hydrolysis of BiI_3 to form basic $Bi(OH)_3$ and the subsequent substitution of I^- by OH^-. For the substitution processes, although the precipitates were washed thoroughly with deionized water, the initial pH values of the reaction systems were different and increased with the increase of the precipitation pH values (**Table 3**). As the OH^- substitution process proceeded involving with the release of I^-, which resulted in the rise of the pH value of the reaction system, the substitution extent was induced with the increase of the precipitation pH value. From the above considerations, the iodine contents in the as-prepared bismuth oxyiodides decreased gradually and the compositions of bismuth oxyiodides changed from tetragonal BiOI to monoclinic Bi_5O_7I, then to α-Bi_2O_3. Besides, the initial molar ratio (Bi/I) of the reaction systems was different and increased with the increase of the precipitation pH values (in **Table 4**). As the OH^- substitution process proceeded in concern with the release of I^-, which resulted in the increase of the pH value of the hydrothermal reaction system, the substitution extent was induced with the increase of the precipitation pH value. At high molar ratio with all the above considerations, the iodine contents in the as-prepared bismuth oxyiodides decreased gradually and the compositions of the bismuth oxyiodides changed from tetragonal BiOI to monoclinic Bi_5O_7I, then to α-Bi_2O_3. But, at low molar ratio, the iodine contents in the as-prepared bismuth oxyiodides decreased gradually and the compositions of the bismuth oxyiodides changed from tetragonal BiOI to monoclinic Bi_5O_7I.

The possible processes for the formation of bismuth oxyiodides are explained as follows [Eqs. (1) – (8)]:

$2\ Bi(OH)_3\ (s) + I^- \rightarrow BiOI\ (s) + H_2O + OH^-$ (1)

$Bi^{3+} + 3\ I^- \rightarrow BiI_3\ (s)$ (2)

$BiI_3\ (s) + 2\ OH^- \rightarrow BiOI\ (s) + 2\ I^- + H_2O$ (3)

$4\ BiOI\ (s) + 2\ OH^- \rightarrow Bi_4O_5I_2\ (s) + 2\ I^- + H_2O$ (4)

$7\ Bi_4O_5I_2\ (s) + 2\ OH^- \rightarrow 4\ Bi_7O_9I_3\ (s) + 2\ I^- + H_2O$(5)

$3\ Bi_7O_9I_3\ (s) + 2\ OH^- \rightarrow 7\ Bi_3O_4I\ (s) + 2\ I^- + H_2O$ (6)

$5\ Bi_3O_4I\ (s) + 2\ OH^- \rightarrow 3\ Bi_5O_7I\ (s) + 2\ I^- + H_2O$ (7)

$2\ Bi_5O_7I\ (s) + 2\ OH^- \rightarrow 5\ Bi_2O_3\ (s) + 2\ I^- + H_2O$ (8)

These equations revealed that BiOI was formed at the beginning of the hydrothermal reaction, and then OH^- gradually substituted I^-in the basic conditions, which resulted in the reduced content of I^- in the samples. Increasing the pH to gradually acquire BiOI, $Bi_4O_5I_2$, $Bi_7O_9I_3$, Bi_5O_7I, and α-Bi_2O_3, the higher the pH value appeared the lower the I^- content in the samples, until the content of I^- in the products was fully replaced by OH^- and finally resulted in the formation of α-Bi_2O_3 under strong basic conditions. However, pure BiOI was the exclusive phase at pH 1, molar ratio 5/10 and 5/25. A competitive relationship typically existed in between the hydroxide and iodide ions in basic solution. By controlling the pH of the hydrothermal reaction, different compositions of bismuth oxyiodides were acquired.

It was found that, with the increase of hydrothermal temperature (or molar ratio (Bi/I)) ranging from 130 to 280 °C (or 5/25 to 5/1), a gradual change in the crystal phase of the reflection peaks took place slightly, which showed a generation in the crystal phase from BiOI to α-Bi_2O_3 at different reaction temperature.

3.1.2 SEM-EDS analysis

Bismuth oxyiodides were synthesized with Bi $(NO_3)_3$•$5H_2O$ and KI by the hydrothermal method at 130-280 °C for pH = 1-14. The surface compositions and morphologies of the samples were observed by FE-SEM-EDS (**Figure 3** and **Table 5**). The FE-SEM image displayed that the morphologies of the samples acquired at different pH values turned from irregular particles to irregular thin-sheets and thin-plates and then became irregular rods (**Figure 3**). These samples showed irregular nanoplate and nanosheet shapes with a lateral size of several micrometers and a thickness between 5 and 40 nm. Samples B5I2-10-280 and B5I2-11-280 exhibited a rod-like irregular shape with a lateral size of several micrometers.

Table 5. Physical and chemical properties of bismuth oxyiodide.

	EDS element atomic ratio (%)			Energy Gap (eV)
	Bi	**O**	**I**	
B5I2-1-280	28.60	71.10	0.28	3.136
B5I2-2-280	29.77	65.15	5.08	1.860
B5I2-3-280	26.22	69.96	3.82	2.112
B5I2-4-280	22.98	70.20	6.82	1.908
B5I2-5-280	25.46	73.81	0.74	2.589
B5I2-6-280	25.05	66.02	8.92	2.226
B5I2-7-280	31.34	59.07	9.59	2.064
B5I2-8-280	25.70	70.69	3.61	2.348
B5I2-9-280	32.03	58.19	9.78	2.441
B5I2-10-280	38.83	53.31	7.86	2.174
B5I2-11-280	27.64	70.70	1.66	2.904
B5I2-12-280	30.28	65.06	4.66	2.371
B5I2-13-280	29.79	66.42	3.80	2.526
B5I2-14-280	33.63	66.20	0.17	2.600

From **Table 5**, the EDS results demonstrated that the main elements of these samples were iodine, bismuth, and oxygen under different pH values. The Bi/I atomic ratios of the bismuth oxyiodide samples were within the range of 1.13-197.82, which corresponded to BiOI/$Bi_4O_5I_2$, BiOI/$Bi_4O_5I_2$/$Bi_7O_9I_3$, $Bi_7O_9I_3$/Bi_5O_7I, Bi_5O_7I/α-Bi_2O_3, and α-Bi_2O_3 phase, compared to the stoichiometric ratio (Bi: I = 1, 2, 2.3, 5, ∞), and could be selectively synthesized through a hydrothermal method. The possible processes for the synthesis of bismuth oxyiodides were described as Eqs. 1 – 8. The EDS result demonstrated that the possible processes for the synthesis of bismuth oxyiodides were explained as Eqs. 1 – 8, which were consistent with the previous result by XRD analyses.

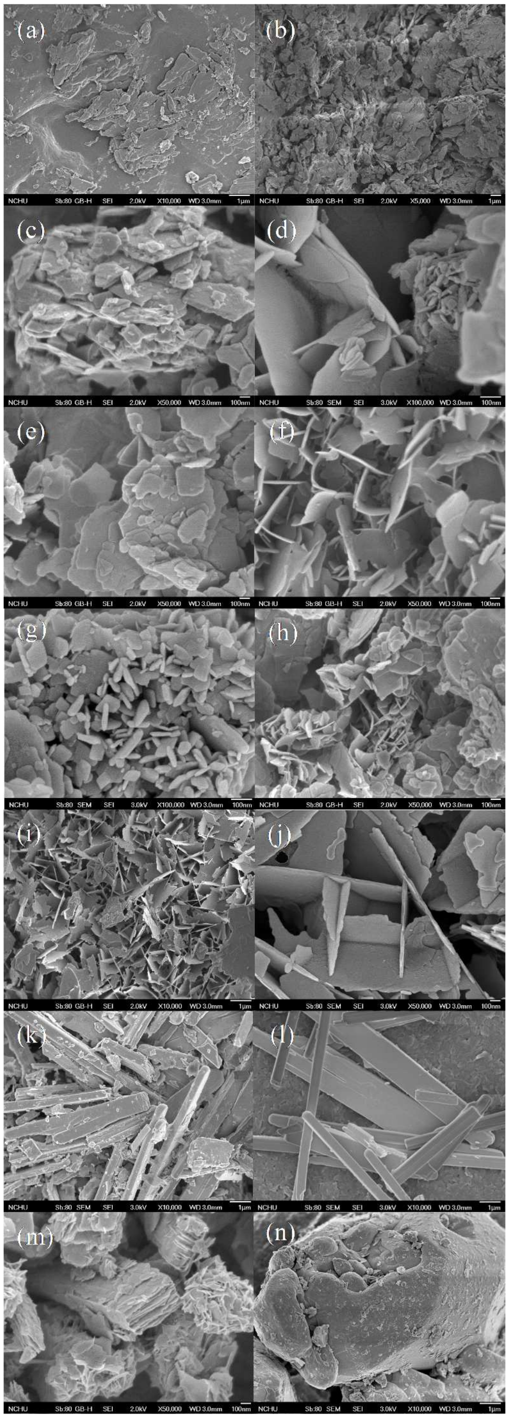

Figure 3. SEM images of bismuth oxyiodide prepared by the hydrothermal autoclave method at different pH value. (Molar ratio $Bi(NO_3)_3$/KI =5/2, hydrothermal conditions: pH = 1-14, temp = 280°C, time = 12 h)

3.1.3 XPS analysis

XPS was used for examining the purity of the synthesized bismuth oxyiodides, and the spectra are displayed in **Figures 4-5**. **Figure 4-5** display the total survey spectra of Bi 4f, I 3d, O1s, and C 1s XPS of the four samples. The characteristic binding energy value of ~157.6 eV for Bi $4f_{7/2}$ (Figure 4b) showed a trivalent oxidation state for bismuth. An additional spin–orbit doublet with binding energy of 155.7 eV for Bi $4f_{7/2}$ was also revealed in all samples, suggesting that certain parts of bismuth existed in the (+3-x) valence state. This showed that the trivalent bismuth partially reduced to the lower valence state by the hydrothermal method. A similar chemical shift of approximately 2.4-2.6 eV for Bi $4f_{7/2}$ was also published by Liao *et* al.[46] They summarized that Bi $^{(+3-x)}$ formal oxidation state could most probably be ascribed to the sub-stoichiometric forms of Bi within the Bi_2O_2 layer, and the formation of the low oxidation state resulted in the oxygen vacancy in the crystal lattice. However, it was supposed in this study that Bi $^{(+3-x)}$ formal oxidation state could most likely be ascribed to the sub-stoichiometric forms of Bi at the outer site of the particles, and the formation of the low oxidation state resulted in the oxygen vacancy in the crystal surface. The binding energy of ~629.4 eV and ~617.9 eV were attributed to I $3d_{5/2}$ and $3d_{3/2}$ respectively, which could be pointed to I at the monovalent oxidation state. **Figure 5** shows the total survey spectra of Bi 4f, I 3d, and O1s XPS of the three pure bismuth oxyiodides and one α-Bi_2O_3 sample. From Figure 5, the observation of the transition peaks involving in the Bi 4f, I 3d, O 1s, and C 1s orbitals demonstrated that the catalysts were composed of the elements of C, O, Bi, and I.

In the pure BiOI, $Bi_7O_9I_3$, and Bi_5O_7I samples, two sets of peaks centered at 160.9 eV, 156.1eV and 163.2 eV, 158.8 eV, could be characteristic of the Bi $^{(+3-x)}$ and Bi $^{3+}$ formal oxidation state of Bi $4f_{5/2}$ and Bi $4f_{7/2}$, and pure α-Bi_2O_3, only two strong peaks centered at 163.7 and 158.2 eV, could be characteristic of the Bi $4f_{5/2}$ and Bi $4f_{7/2}$, revealing that the main chemical states of the bismuth element in the samples were trivalent.

3.1.4 FT-IR analysis

To investigate the chemical composition and chemical bonding of composites, the FT-IR investigation was carried out. **Figure 6** shows the FT-IR spectra produced under different bismuth oxyiodides, where the strong absorption mainly located in the 400–700 cm^{-1}, as a result of the stretching vibrations of Bi−O, Bi−O−I, and Bi−O−Bi in bismuth oxyiodides. [47] At the same time, the ν(C−O) at 1386 cm^{-1} and ν(C−O) at 1462 cm^{-1} corresponded to the very weak characteristic peaks of CO_3^{2-}.

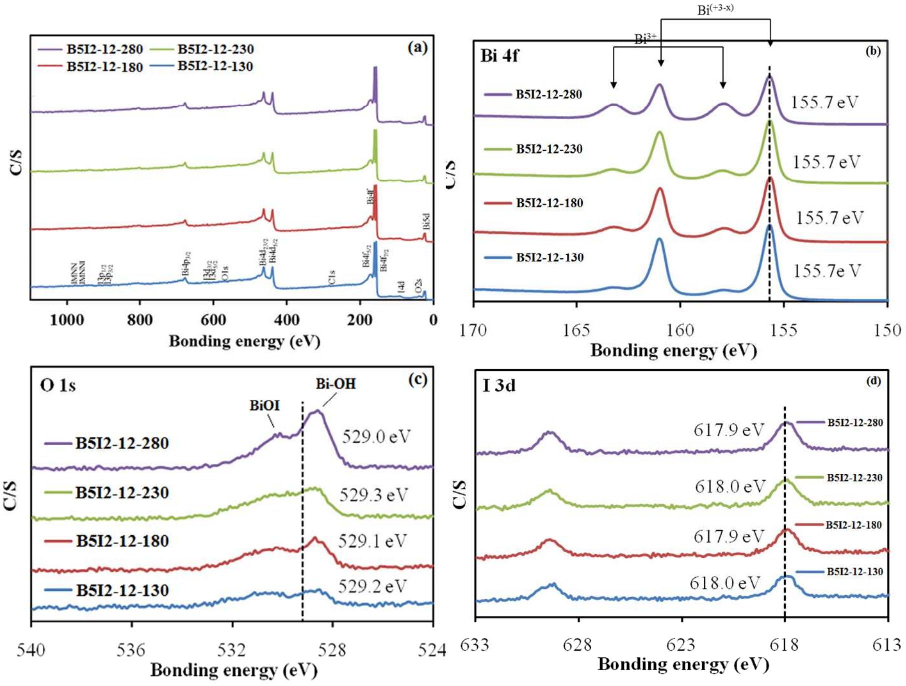

Figure 4. High-resolution XPS spectra of the bismuth oxybromide prepared by the hydrothermal autoclave method at 130, 180, 230, 280 ˚C, 12 h, pH= 12. (a) Total survey; (b) Bi 4f; (c) O 1s; (d) I 3d.

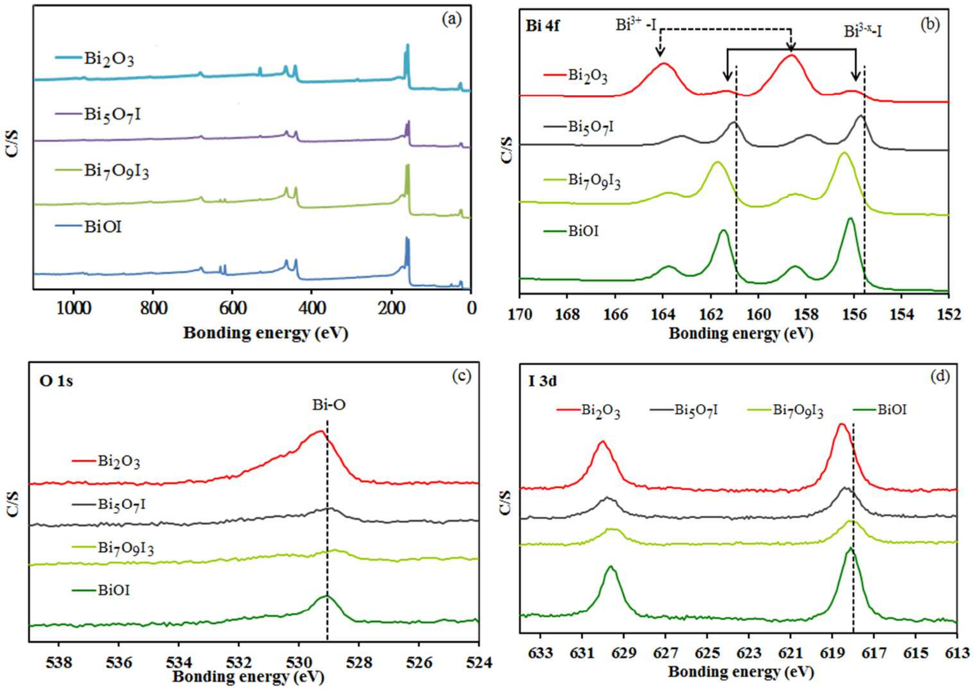

Figure 5. High-resolution XPS spectra of the bismuth oxyiodide prepared by the hydrothermal autoclave method. (a) Total survey; (b) Bi 4f; (c) O 1s; (d) I 3d.

Therefore, it could be concluded that the samples were composed of bismuth oxyiodides. Besides, no impurity or solvent residue absorption peak or absorption band was detected.

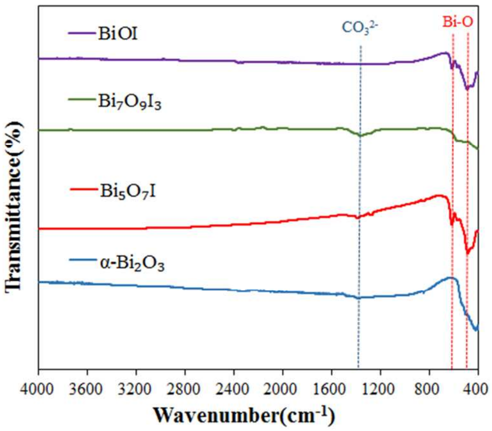

Figure 6. UV-vis absorption spectra of the different bismuth oxyiodide catalysts.

3.1.5 UV–vis diffuse reflectance spectroscopy

The UV–vis adsorption spectra of the prepared samples are displayed in **Figure 7** and **Figure S4-S5** (ESI†). Their corresponding band gap energy was estimated, which was close to 1.860-3.136 eV (**Table 5**). Under visible light irradiation, compared to P25, bismuth oxyiodides showed pronounced light absorbance abilities at λ > 400 nm, suggesting their potential photocatalytic activity. The steep shape and strong absorption in the visible-light region attributed the visible-light absorption to the intrinsic band gap transition between the valence band and the conduction band, rather than the transition from the impurity levels.[48] The difference of band gap energy in the synthesized bismuth oxyiodide could be attributed to their individual composition with various characteristics. Based on **Table 5 and 6**, the photocatalytic activities were not mainly attributed to different absorption abilities of visible light due to the different band gap energy.

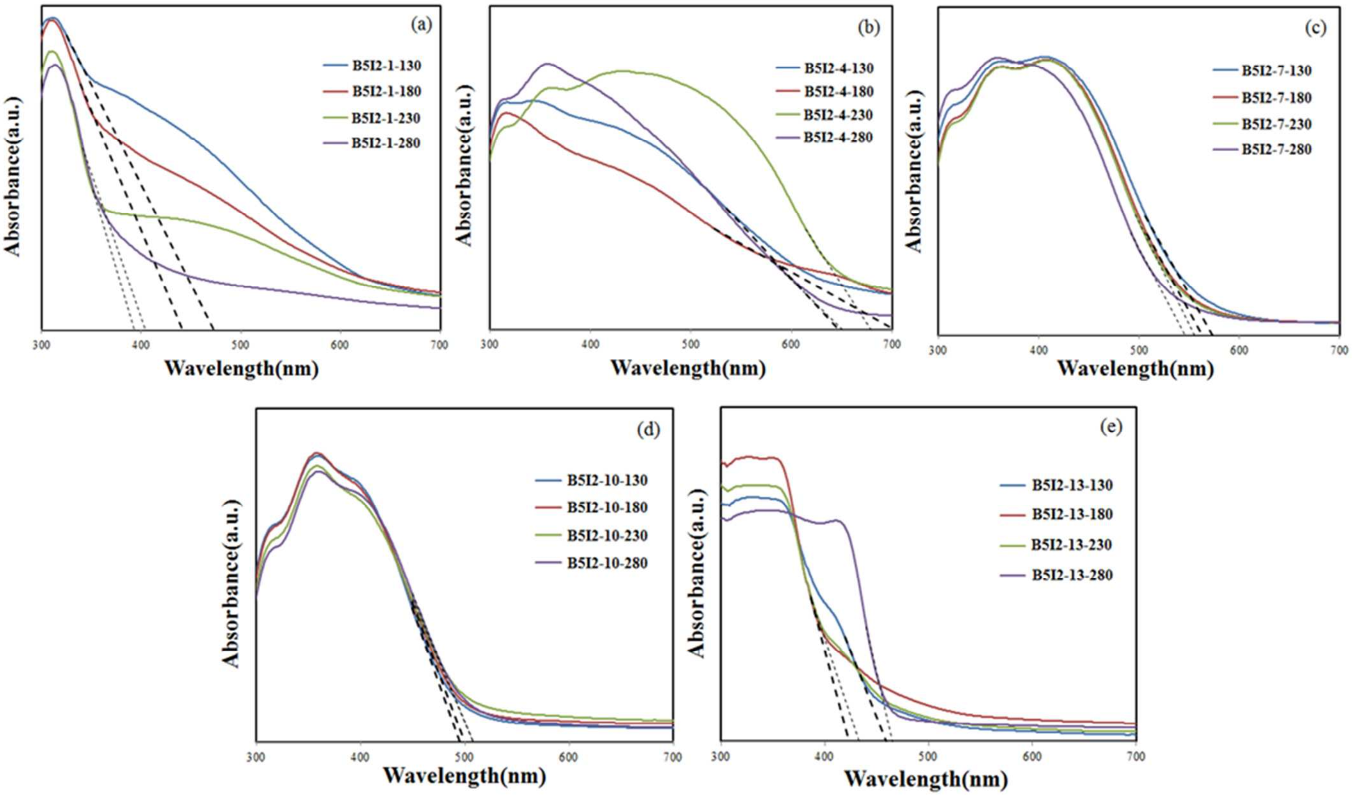

Figure 7. UV-vis absorption spectra of the prepared bismuth oxyiodide catalysts under different pH values and reaction temperature. (Molar ratio $Bi(NO_3)_3$/KI =5/2, reaction time 12h).

3.1.6 BET surface areas

The BET of the bismuth oxyiodides was about 0.08-7.20 m^2/g, respectively. This nanoplate and nanosheet structure could provide efficient transport paths for reactants and more active sites for the photocatalytic reaction. The structure was also advantageous to efficient photo-energy reaping and introducing the separation of electron-hole pairs, thus encouraging the photocatalytic abilities.

It is understood that the size of nanoparticles has significant effects on photo-catalytic properties because of the variation of surface area, number of active sites and so forth.[48] The smaller particle size of nanoparticles would cause a larger surface area (more active sites) to improve the photocatalytic abilities. Besides, the band-gap energy is also related to the photocatalytic abilities.[50] The lower band-gap has a positive effect on the photocatalytic abilities because the lower source energy is needed for stimulating a photocatalytic reaction. It means that less energy is needed for activating the nanoparticles to generate excited electron/hole pairs and then induce photocatalytic reactions. In this study, the particle sizes of bismuth oxyiodides were a little higher than those of P25-TiO_2; however, the result of band-gap was on the opposite. It suggested that the higher photocatalytic abilities of bismuth oxyiodides than P25-TiO_2 could be attributed to a lower band-gap, which would promote to generate more excited electron-hole pairs to enhance the photocatalytic abilities.

3.2 Evaluation of Photocatalytic Ability

3.2.1 Photocatalytic Ability

The photocatalytic ability of the samples was evaluated by degrading CV (or SA) under visible light (or UV) irradiation with 0.5 g/L of photocatalyst added. The degradation ability as a function of reaction time is displayed in **Figure 8** and **Figure S6-S7** (ESI[†]). In the absence of photocatalysts, CV (or SA) could not be degraded under visible (or UV) light irradiation. The removal efficiency was improved significantly in the presence of bismuth oxyiodides. After 24 h irradiation, bismuth oxyiodides revealed superior photocatalytic activities, with the CV removal efficiency up to 99.9%. The UV–vis adsorption spectra of prepared samples (**Figure 7** and **Figure S4-S5** (ESI[†])) corresponding band gap energy were estimated, which were close to 1.860-3.136 eV (**Table 5**). Under visible light irradiation, compared to P25, bismuth oxyiodides showed pronounced light absorbance abilities at $\lambda > 400$ nm, suggesting their potential photocatalytic activities. The steep shape and strong absorption in the visible-light region attributed the visible-light absorption to the intrinsic band gap transition between the valence band and the conduction band, rather than the transition from the impurity levels. Therefore, compared to UV irradiation, bismuth oxyiodides showed superior photocatalytic performance under visible light irradiation.

To further understand the reaction kinetics of CV photocatalytic degradation, the apparent pseudo-first-order model [41] described in the equation $\ln(C_o/C) = kt$ was used in the photocatalytic experiments. By using the first-order linear fit of the data from **Tables 6-7**, the k value of B5I2-7-280 ($Bi_7O_9I_3$) was acquired as the maximum degradation rate of $2.225 \times 10-1\ h^{-1}$, and this value was considerably higher than that of the other samples. The activity of $Bi_7O_9I_3/Bi_5O_7I$ was higher than those of P25-TiO_2, BiOI, $Bi_4O_5I_2$, $Bi_7O_9I_3$, Bi_5O_7I, and α-Bi_2O_3.

The superior photocatalytic activity of bismuth oxyiodide composites might be attributed to its efficient usage of visible light and the high separation efficiency of the electron-hole pairs with its hieratical structure. The $Bi_7O_9I_3/Bi_5O_7I$ composite with a largest S_{BET} did exhibit the highest photocatalytic ability among all the samples, suggesting that changes in the photocatalytic ability were associated with the BET surface area.

Table 6. The pseudo-first-order rate constants for the degradation of CV with bismuth xxyiodide photocatalysts under visible light irradiation.

pH value	Temperature(℃)							
	130		180		230		280	
	k (h^{-1})	R^2	k (h^{-1})	R^2	k (h^{-1})	R^2	k (h^{-1})	R^2
1	0.0025	0.9719	0.0017	0.9508	0.0011	0.9513	0.0036	0.6597
2	0.0033	0.9685	0.0037	0.9758	0.0041	0.9884	0.0058	0.8928
3	0.0070	0.9715	0.0028	0.9533	0.0015	0.9564	0.0217	0.9615
4	0.0014	0.9761	0.0021	0.9542	0.0071	0.9735	0.0362	0.9775
5	0.0058	0.9565	0.0015	0.9679	0.0026	0.9601	0.0120	0.9131
6	0.0594	0.9614	0.0593	0.9663	0.0789	0.9790	0.1950	0.9769
7	0.0651	0.9552	0.0238	0.9775	0.0435	0.9511	0.2225	0.8881
8	0.0243	0.9518	0.0205	0.9707	0.0301	0.9520	0.0421	0.9512
9	0.0858	0.9640	0.0577	0.9640	0.0621	0.9690	0.1432	0.9660
10	0.0377	0.9742	0.0220	0.9742	0.0165	0.9748	0.1079	0.9765
11	0.0342	0.9768	0.0361	0.9768	0.0049	0.9620	0.0133	0.9064
12	0.0166	0.9686	0.0174	0.9686	0.0124	0.9604	0.0569	0.9327
13	0.0094	0.9788	0.0134	0.9788	0.0095	0.9671	0.0352	0.9423
14	0.0012	0.9603	0.0035	0.9603	0.0024	0.9578	0.0034	0.9177

Table 7. The pseudo-first-order rate constants for the degradation of CV with bismuth oxyiodide photocatalysts under visible light irradiation.

Bi/I Molar ratio	pH											
	1		4		7		10		13		14	
	k (h^{-1})	R^2	k (h^{-1})	R^2	k (h^{-1})	R^2	k (h^{-1})	R^2	k (h^{-1})	R^2	k (h^{-1})	R^2
5 : 1	0.0070	0.7369	0.0029	0.9272	0.0074	0.8010	0.0399	0.9453	0.0224	0.9566	0.0118	0.9590
5 : 2	0.0056	0.3908	0.0380	0.9738	0.2052	0.8800	0.1041	0.9748	0.0323	0.9329	0.0033	0.9175
5 : 5	0.0521	0.9358	0.0620	0.9797	0.0553	0.8581	0.0740	0.9123	0.0281	0.9413	0.0095	0.9314
5 : 10	0.0462	0.9036	0.1295	0.9327	0.1170	0.9576	0.1063	0.9187	0.0318	0.9835	0.0205	0.8412
5 : 25	0.0411	0.9613	0.0861	0.9439	0.0738	0.9648	0.1162	0.9147	0.0320	0.9682	0.0150	0.8981

In the absence of photocatalysts, CV could not be degraded under visible light irradiation; the superior photocatalytic ability of bismuth oxyiodides could be attributed to its efficient use of visible-light and the highly effective separation of electron–hole pairs within its samples.

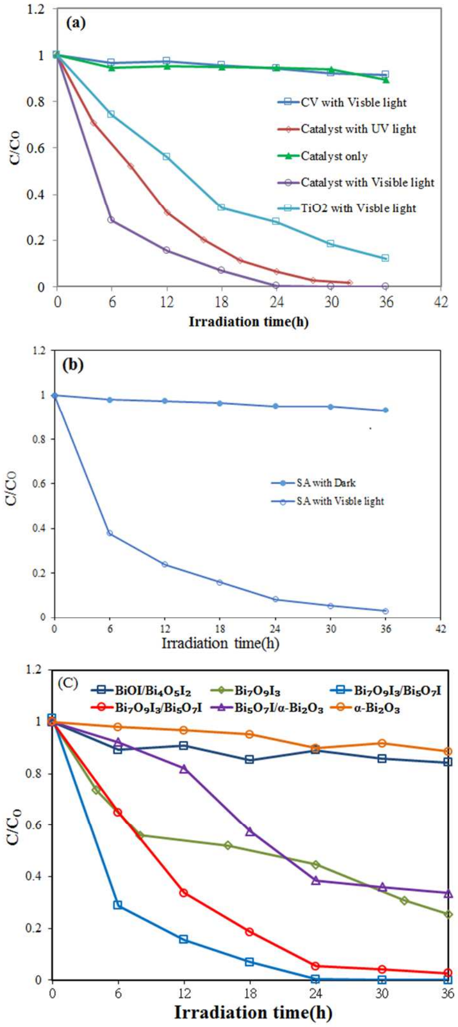

Figure 8. Photocatalytic degradation of CV and SA by the resulting bismuth oxyiodide catalysts and the control experiments under simulated visible light irradiation. (a) CV; (b) SA; (c) pH = 1-14. (Molar ratio $Bi(NO_3)_3$/KI =5/2, Temp = 280˚C, Time=12 h)

The evaluated durability of the $Bi_7O_9I_3/Bi_5O_7I$ composite was measured by recycling the used catalyst. After each cycle, the catalyst was collected by centrifugation. No apparent loss was observed in the photocatalytic ability when CV was degraded in the third cycle; even during the sixth run, the decrease in the photocatalytic efficiency was 1.5% (**Figure 9(a)**). The used $Bi_7O_9I_3/Bi_5O_7I$ composite was also measured using XRD, and no detectable difference was showed between the as-prepared and the used samples (**Figure 9(b)**); thus, the $Bi_7O_9I_3/Bi_5O_7I$ composite had high photo-stability.

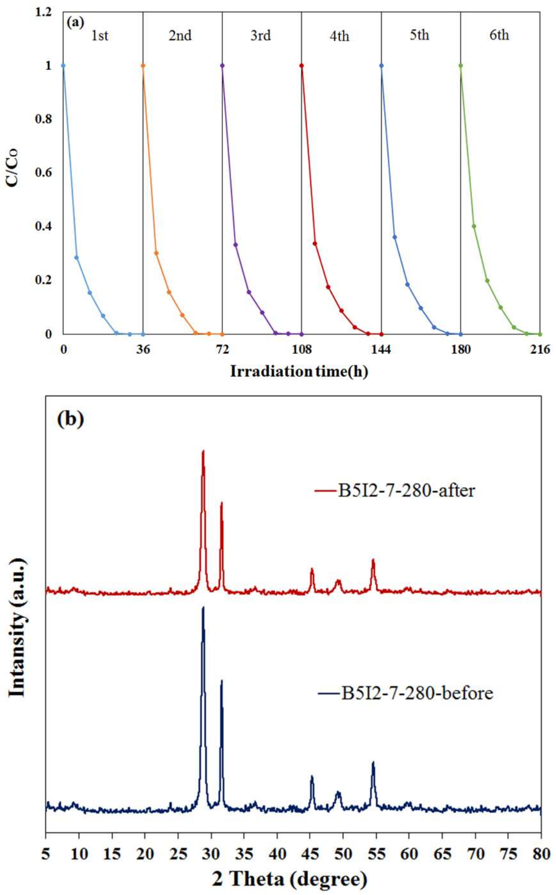

Figure 9. (a) Cycling runs and (b) XRD patterns acquired before and after in the photocatalytic degradation of CV in the presence of B5I2-7-280.

The degradation efficiency as a function of reaction time is illustrated in **Figure S6-S7** of ESI†. The removal efficiency was enhanced significantly in the presence of BiO_pBr_q/BiO_mI_n catalysts. After 48h irradiation, BiO_pBr_q/BiO_mI_n showed superior photocatalytic performance, with CV removal efficiency up to 99%. To further understand the reaction kinetics of CV degradation, the apparent pseudo-first-order model [21] expressed by the $\ln(C_o/C) = k_{app}t$ equation was applied in this experiments. Via the first-order linear fit from the data of **Figure S6-S7** shown in **Table 3**, k_{app} of BB1I2-4-110-12 was obtained at the maximal degradation rate of 5.285×10^{-1} h^{-1}, greatly higher than the others composites. Therefore, the $Bi_4O_5Br_2/BiOI$ composite showed the best photocatalytic activity. The result showed that the $Bi_4O_5Br_2/BiOI$ composite was a much more effective photocatalyst than the others. The superior photocatalytic ability of BiO_pBr_q/BiO_mI_n might be ascribed to its efficient utilization of visible light and the high separation efficiency of the electron-hole pairs with its composites.

The durability of the $Bi_4O_5Br_2/BiOI$ (BB1I2-4-210-12) composite was evaluated through the recycle of the used catalyst. There was no apparent loss of photocatalytic activities in removing crystal violet in the fifth cycle, and even in the tenth run, the declination in photocatalytic activities was less than 3% (**Figure 8 (a)**). The used $Bi_4O_5Br_2/BiOI$ was also examined by XRD, and there was no detectable difference between the as-prepared and the used samples (**Figure 8 (b)**). Therefore, it could be deduced that the $Bi_4O_5Br_2/BiOI$ composite had good photostability.

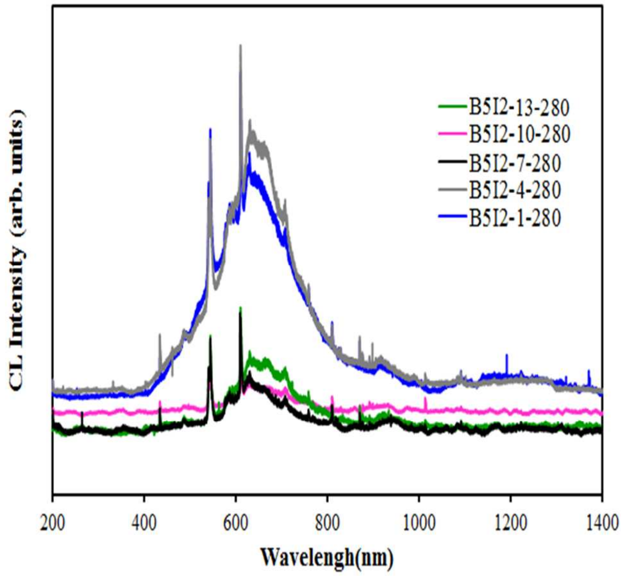

Figure 10. Photoluminescence spectra of bismuth oxyiodide under hydrothermal conditions. (Hydrothermal conditions: Molar ratio $Bi(NO_3)_3/KI = 5/2$, pH = 1-14, temp = 280 °C, time = 12h)

3.2.2 Photoluminescence spectra

The PL spectra were used for searching the recombination rate of the photogenerated electron–hole pairs. [52] To research the separation capacity of the photo-generated carriers in the heterostructures, the PL spectra of bismuth oxyiodides were detected; the results are displayed in **Figure 10**. A strong emission peak appeared at approximately 620 nm for bismuth oxyiodides, and it might have been acquired from the direct electron–hole recombination of band transitions. However, the characteristic emission peak at approximately 620 nm nearly vanished for bismuth oxyiodides, showing that the recombination of photogenerated charge carriers was greatly inhibited. The efficient separation of charge might increase the lifetime of charge carriers and enhance the efficiency of interfacial charge transfer to the adsorbed photocatalysts, thus improving the photocatalytic ability. [46] The low relative PL intensity of band B5I2-7-280 photocatalysts, as illustrated in **Figures 10**, suggested the possession of the lowest recombination rate of electron–hole pairs, resulting in the higher photocatalytic ability, as illustrated in **Figure 8** and **Tables 6-7**. Under visible light irradiation, the photocatalytic activities followed the order of $Bi_7O_9I_3$ > $Bi_7O_9I_3/Bi_5O_7I$ > $BiOI/Bi_4O_5I_2/Bi_7O_9I_3$ > $Bi_7O_9I_3/Bi_2O_3$ > $BiOI/Bi_4O_5I_2$, which was mainly attributed to the recombination rate of electron–hole pairs. Therefore, it showed that the recombination rate of electron–hole pairs was the major factor in the photocatalytic degradation of CV dye.

3.3 Photodegradation mechanisms of CV

Various primary active species, such as hydroxyl radicals ($HO^{\bullet}$), photogenerated hole (h^+), superoxide radicals ($O_2^{-\bullet}$) and singlet oxygen ($^1O_2$), could be created during the photocatalytic degradation processes in the UV-vis/bismuth oxyiodide system.[10] Ye and his coworkers revealed that the rhodamine photodegradation by BiOI under visible-light was dominated by $O_2^{-\bullet}$ and h^+ oxidation being the main active species. [53] Xu et al. proposed that the hydroxyl radicals and direct holes were the primary reactive species in the benzotriazole degradation by BiOBr spheres under simulated solar light irradiation.[20] Ge and Zhang investigated the pathway for generating active oxygen radicals ($O_2^{-\bullet}$ and $^{\bullet}OH$) on the surface of $In(OH)_xS_y$ for the degradation of RhB.[54] Wang's group showed that high efficient visible-light-driven sodium pentachlorophenate removal with Bi_3O_4Br could be attributed to the effective separation and the transfer of photoinduced charge carriers in Bi_3O_4Br with narrower band-gap and more negative conduction band position, which favored the photogenerated electrons trapping with molecular oxygen to produce $O_2^{-\bullet}$.[55] Wang et al. proposed that the $^{\bullet}$OH radical was generated by multistep reduction $O_2^{-\bullet}$.[56] The generation of $O_2^{-\bullet}$ radicals could not only inhibit the recombination of photoinduced charge carriers, but also advantage the dechlorination of chlorinated phenol derivative. The HO$^{\bullet}$ radical might only be generated via an $e^- \rightarrow O_2^{-\bullet} \rightarrow H_2O_2 \rightarrow {}^{\bullet}OH$ pathway. Meanwhile, $^{\bullet}$OH radicals were generated by multistep reduction $O_2^{-\bullet}$ in the system. In a valence band of Bi(III), holes formed by photoexcitation were regarded as Bi(V).[57]

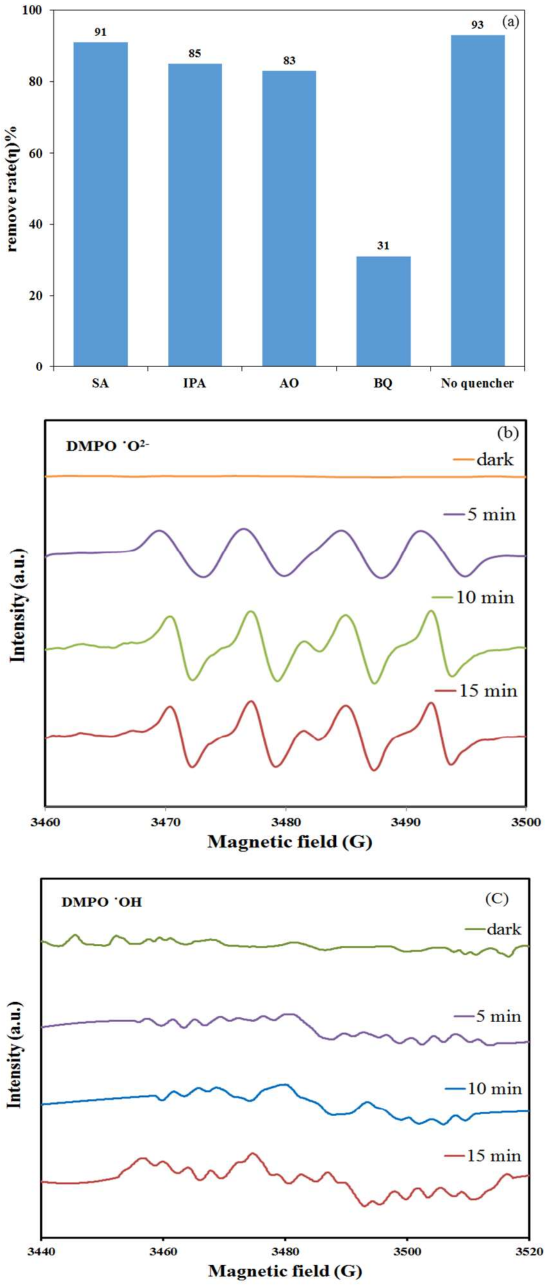

Figure 11. (a) The dye concentration during photodegradation as a function of irradiation time observed in bismuth oxyiodides under the addition of different scavengers: SA, IPA, AQ, and BQ; (b) (c) DMPO spin-trapping EPR spectra for DMPO-O_2^- and DMPO-OH under visible light irradiation with bismuth oxyiodides.

The standard redox potential of Bi5+/Bi3+ was more negative than it of OH$^{\bullet}$/OH$^-$.[58] Accordingly, photogenerated holes on the surface of bismuth oxyhalides were not supposed to react with OH^-/H_2O to form $^{\bullet}$OH, suggesting that the decomposition of rhodamine [59] and bisphenol-A [60] could be attributed to a direct reaction with the photogenerated holes or with superoxide radicals (generated by the excited electron) or both species. Zhu *et al.* revealed that photocatalytic reactions in the presence of nitrogen gas and the radical scavenger suggested $^{\bullet}$OH and $O_2^{-\bullet}$ being two main actives in the whole degradation process.[61] According to earlier studies, [62] the dominant active oxygen species generated in direct oxidation and photocatalytic reactions were $^1O_2$ and $^{\bullet}$OH radicals, respectively. Moreover, in this visible-light-induced semiconductor system, hydroxylated compounds were also separated and identified for the photocatalytic degradation of Ethyl Violet [63] and CV. On the basis of above mentions, it was proposed that the probability for the formation of $^{\bullet}$OH radicals should be much lower than it for $O_2^{-\bullet}$ radicals. However, the $^{\bullet}$OH radical was an extremely strong, non-selective oxidant, which led to the partial or complete mineralization of several organic compounds.

To evaluate the effect of the active species during the photocatalytic degradation, a series of quenchers were added to scavenge the relevant active species. The $^{\bullet}$OH, $O_2^{\bullet-}$, $^1O_2$, and h^+ were examined by adding 1.0 mM isopropanol (a quencher of $^{\bullet}$OH),[64] 1.0 mM benzoquinone (a quencher of $O_2^{\bullet-}$),[65] 1.0 mM sodium azide (a quencher of $^1O_2$),[66] and 1.0 mM ammonium oxalate (a quencher of h^+) ,[67] respectively.

As shown in **Figure 11**(a), the degradation efficiency of isopropanol quenching decreased more than that of ammonium oxalate, and the degradation efficiency of benzoquinone quenching decreased more than that of isopropanol, but the photocatalytic degradation of CV was not affected by the addition of sodium azide. In brief, the quenching effects of various scavengers revealed that the reactive $O_2^{\bullet-}$ played a major role, and $^{\bullet}$OH or h^+ played a minor role in the CV degradation. **Figure 11**(b)(c) show that no EPR signal was examined when the reaction was accomplished in the dark, while the signals with intensity corresponding to the characteristic peak of DMPO-OH and DMPO-O_2^- adducts [23] were showed during the reaction process under visible light irradiation. Besides, the intensity gradually increased with the prolonged reaction time, proposing that the $O_2^{\bullet-}$ (major active species) and the $^{\bullet}OH$ (minor active species) were generated in the presence of bismuth oxyiodides and oxygen under visible light irradiation. Chen's group proposed [68] that Pt/TiO_2 gathered less negative species on catalyst surfaces, which declined reaction rates, than pure TiO_2 did in an acidic environment. The $^{\bullet}OH$ radicals were produced subsequently, as also expressed in eqs.9-14.

$$O_2^{-\bullet} + H^+ + e^- \rightarrow HOO^{\bullet} \quad (9)$$
$$HOO^{\bullet} + H_2O \rightarrow {}^{\bullet}OH + H_2O_2 \quad (10)$$
$$O_2^{-\bullet} + 2H^+ \rightarrow H_2O_2 \quad (11)$$
$$H_2O_2 + e^- \rightarrow {}^{\bullet}OH + OH^- \quad (12)$$
$$h^+ + OH^- \rightarrow {}^{\bullet}OH \quad (13)$$
$$h^+ + H_2O \rightarrow {}^{\bullet}OH + H^+ \quad (14)$$

These cycle reactions continuously happened when the system was exposed to the visible-light irradiation. Finally, after several cycles of photo-oxidation, the photocatalytic degradation of CV by the generated oxidant species could be shown by the eqs.15-16:

$$CV + OH^{\bullet} \rightarrow \text{degraded compounds} \quad (15)$$
$$CV^{+\bullet} + OH^{\bullet} \rightarrow \text{degraded compounds} \quad (16)$$

It was reported that a mechanism of dye sensitized degradation exhibited in the degradation of dye.[61,68,69] This photocatalytic degradation was also ascribed to the photodegradation of CV by the photocatalytic route of CV photosensitized bismuth oxyiodides. CV absorbing a visible photon was promoted to an excited electronic state CV*, from which an electron could be transferred into the conduction band of photocatalysts.

$$CV + h\nu \rightarrow CV^* \quad (17)$$
$$CV^* + BiO_xI_y \rightarrow CV^+ + BiO_xI_y\,(e^-) \quad (18)$$
$$O_2 + e^- \rightarrow O_2^{-\bullet} \quad (19)$$

Once the electron reached the conduction band of bismuth oxyiodides, it induced the formation of active oxygen species, which caused the degradation of CV dye. It was clear that, except for the photodegradation of CV by the route of bismuth oxyiodide-mediated and photosensitized processes, another type of photocatalytic route accounted for the enhanced photocatalytic activity. Both the photosensitized and photocatalytic processes proceeded concurrently (**Figure 12**). However, in photosensitized and photocatalytic reaction conditions, $O_2^{\bullet-}$ radicals were generated by the reaction of photogenerated and photosensitized electron with oxygen gas on the photocatalyst surface, and $^{\bullet}OH$ radicals were also generated by the reaction of $O_2^{\bullet-}$ radicals with H^+ ion and hole h^+ with OH^- ion (or H_2O). The $^{\bullet}OH$ radical was produced subsequently, as expressed in Eqs. (9) to (14).

Under visible irradiation, temporal variations occurring in the solution of CV dye during the degradation process were detected by the HPLC-PDA-MS. Given the CV irradiation up to 24 h at pH 4, the chromatograms were displayed in **Figure S8** of ESI† and recorded at 580, 350, and 300 nm, and nineteen intermediates were separated and identified, with the retention time under 50 min. The CV dye and its related intermediates were marked as species **A-J**, **a-f**, and **α-γ**. Except for the initial CV dye (peak A), the peaks initially increased before the subsequent decrease, indicating the generation and transformation of the intermediates.

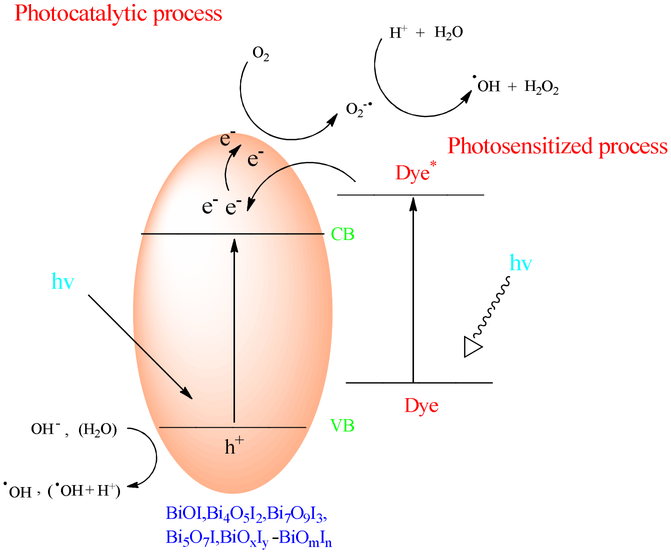

Figure 12. The band structure diagram of bismuth oxyiodide photocatalysts and the possibile charge separation processes.

The maximum absorption of the spectral bands shifted from 588.9 nm (spectrum A) to 542.0 nm (spectrum J), from 377.8 nm (spectrum a) to 340.3 nm (spectrum f), and from 311.2 nm (spectrum α) to 281.2 nm (spectrum γ) in **Figure S9** of ESI†. The maximum adsorption in the UV-vis spectral region of each intermediate is listed in **Table S1** (ESI†). They were separated and identified as **A-J** **a-f**, and **α-γ**, respectively corresponding to the peaks A-J, a-f, and α-γ in three chromatographs (**Figure S8** of ESI†**)**. These shifts of the absorption band were supposed to result from the generation of a series of *N*-de-methylated intermediates. From these results, several groups of intermediates could be differentiated. The intermediates were further identified using the HPLC-ESI-MS, and the relevant mass spectra are showed in

Figures S10 and **Table S1** of ESI[†]. The molecular ion peak appeared in the acid form of the intermediates using the HPLC-ESI-MS. The detailed data of intermediates are described in the appendix A.

In previous reports,[63,69,70] the *N*-de-alkylation processes were preceded by the generation of a nitrogen-centered radical while the oxidative degradation was preceded by the formation of a carbon-centered radical in the photocatalytic degradation of triarylmethane dye. In the experimental results, the dye degradation mechanism was tentatively proposed, described in **Figure S11-S13**. The excited dye injected an electron into the conduction band of photocatalysts, where it was scavenged by O_2 gas to form $O_2^{-\bullet}$ radicals. De-methylation of CV occurred mostly by attack by the active species, which was a perfect nucleophilic reagent, on the *N*-methyl portion of CV. Further, $O_2^{-\bullet}$ radicals subsequently reacted with H_2O to generate $^{\bullet}OH$ radicals and the other active species. The probability for the generation of $^{\bullet}OH$ radicals should be much lower than that for $O_2^{-\bullet}$ radicals. The $^{\bullet}OH$ radical was an extremely strong, non-selective oxidant, which led to the partial or complete mineralization of several organic compounds. All the above active species drove the degradation or mineralization of the dye molecule. All the intermediates identified in these two studied topics had the same results under visible light irradiation. There was doubtless that the major oxidant was $^{\bullet}OH$ radicals, not $O_2^{-\bullet}$ radicals.

4. Conclusions

In the current process, the controllable crystal phases and morphologies of bismuth oxyiodides could be accomplished by simply changing some growth parameters, including molar ratio (Bi/I), pH value, and reaction temperature. The results demonstrate that a series of changes in the compounds happen at different hydrothermal conditions, expressed as $BiOI \rightarrow Bi_4O_5I_2 \rightarrow Bi_7O_9I_3 \rightarrow Bi_5O_7I \rightarrow \alpha\text{-}Bi_2O_3$. The bismuth oxyiodide catalysts are of different phases, which degrade nearly 100% of CV from the solution after 24 h under visible light irradiation, and the high activity can be attributed to their relatively efficient utilization of visible light. Both the photosensitized process and the photocatalytic process proceed concurrently for the CV degradation, whereas the photocatalytic process is the only process in the SA degradation. $O_2^{-\bullet}$ radicals are the main active species, and $^{\bullet}OH$ radicals (or h^+) are the minor active species in the photocatalytic process. In the photocatalytic and photosensitized processes, *N*-demethylation and the cleavage of the conjugated CV dye structure occur during the degradation with bismuth oxyiodides as the catalyst. The reaction mechanisms for Vis/bismuth oxyiodides proposed in this research should offer some notion for the applications to the decoloration of dyes.

Acknowledgements

This research was supported by the Ministry of Science and Technology of the Republic of China (NSC-101-2113-M-142-001-MY3).

Notes and references

1 S. Malato, P. Fernández-Ibáñez, M.I. Maldonado, J. Blanco and W. Gernjak, Catal. Today, 2009, **147**, 1-59.

2 M.A. Shannon, P.W. Bohn, M. Elimelech, J.G. Georgiadis, B.J. Marinas and A.M. Mayes, Nature, 2008, **452**, 301-310.

3 W.W. Lee, W.H. Chung, W.S. Huang, W.C. Lin, W.Y. Lin, Y.R. Jiang and C.C. Chen, J. Taiwan Inst. Chem. Eng., 2013, **44**, 660-669.

4 Z. Chen, W. Wang, Z. Zhang and X. Fang, J. Phys. Chem. C, 2013, **117**, 19346−19352.

5 J. Xu, W. Meng, Y. Zhang, L. Li and C. Guo, App. Catal. B, 2011, **107**, 355-362.

6 M.Q. Yang, N. Zhang, M. Pagliaro and Y.J. Xu, Chem. Soc. Rev., 2014, **43**, 8240-8254.

7 N. Zhang, Y. Zhang and Yi-Jun Xu, Nanoscale, 2012, **4**, 5792–5813.

8 M.Q. Yang and Y.J. Xu, Phys. Chem. Chem. Phys., 2013, **15**, 19102-19118.

9 C. Han, M.Q. Yang, B. Weng and Y.J. Xu, Phys. Chem. Chem. Phys., 2014, **16**, 16891-16903.

10 N. Zhang, X. Fu and Y.J. Xu, J. Mater. Chem., 2011, **21**, 8152-8158.

11 Y. Zhang, N. Zhang, Z.R. Tang and Y.J. Xu, Chem. Sci., 2012, **3**, 2812-2822.

12 Z. Chen, N. Zhang and Y.J. Xu, CrystEngComm, 2013, **15**, 3022–3030.

13 Y. Zhang, Z.R. Tang, X. Fu, and Y.J. Xu, ACS Nano, 2010, **4**, 7303-7311.

14 N. Zhang, M.Q. Yang, Z.R. Tang, and Y.J. Xu, ACS Nano, 2014, **8**, 623-633.

15 H. Cheng, B. Huang and Y. Dai, Nanoscale, 2014, **6**, 2009–2026.

16 X. Xiao and W.D. Zhang, J. Mater. Chem., 2010, **20**, 5866–5870.

17 Y. Huo, J. Zhang, M. Miao and Y. Jin, Appl. Catal. B: Environ., 2012, **111-112**, 334-341.

18 L. Ye, J. Chen, L. Tian, J. Liu, T. Penga, K. Deng and L. Zan, Appl. Catal. B: Environ., 2013, **130–131**, 1– 7.

19 X. Chang, J. Huang, C. Cheng, Q. Sui, W. Sha, G. Ji, S. Deng and G. Yu, Catal. Commun., 2010, **11**, 460–464.

20 X. Xiao and W.D. Zhang, RSC Advances, 2011, **1**, 1099–1105.

21 Y. Lei, G. Wang, S. Song, W. Fan, M. Pang, J. Tanga and H. Zhang, Dalton Trans., 2010, **39**, 3273–3278.

22 X. Zhang, Z.H. Ai, F.L. Jia and L.Z. Zhang, J. Phys. Chem. C, 2008, **112**, 747–753.

23 X. Xiao, C. Xing, G. He, X. Zuo, J. Nana and L. Wang, Appl. Catal. B: Environ., 2014, **148–149**, 154–163.

24 X. Xiao, R. Hao, X. Zuo, J. Nan, L. Li and W. Zhang, Chem. Eng. J., 2012, **209**, 293–300.

25 Q.C. Liu, D.K. Ma, Y.Y. Hu, Y.W. Zeng and S.M. Huang, ACS Appl. Mater. Interfaces, 2013, **5**, 11927–11934.

26 S. Sun, W. Wang, L. Zhang, L. Zhou, W. Yin and M. Shang, Environ. Sci. Technol., 2009, **43**, 2005–2010.

27 W.L. Huang and Q.S. Zhu, J. Comput. Chem., 2009, **30**, 183–190.

28 X. Xiao, C. Liu, R. Hu, X. Zuo, J. Nan, L. Li and L. Wang, J. Mater. Chem., 2012, **22**, 22840–22843.

29 X. Xiao, R. Hu, C. Liu, C. Xing, C. Qian, X. Zuo, J. Nan and L. Wang, Appl. Catal. B: Environ., 2013, **140–141**, 433–443.

30 S.T. Huang, Y.R. Jiang, S.Y. Chou, Y.M. Dai and C.C. Chen, J. Mol. Catal. A: Chem., 2014, **391**, 105-120.

31 J. Jiang, X. Zhang, P. Sun and L. Zhang, J. Phys. Chem. C, 2011, **115**, 20555–20564.

32 J. Wang, Y. Yu and L. Zhang, Appl. Catal. B: Environ., 2013, **136–137**, 112–121.

33 C. Chang, L. Zhu, S. Wang, X. Chu and L. Yue, ACS Appl. Mater. Interfaces, 2014, **6**, 5083−5093.

34 Y. Liu, W. Yao, D. Liu, R. Zong, M. Zhang, X. Ma and Y. Zhu, Appl. Catal. B: Environ, 2015, **163**, 547-553.

35 H. Huang, K. Liu, Y. Zhang, K. Chen, Y. Zhang and N. Tian, RSC Adv., 2014, **4**, 49386-49394.

36 D.F. Duxbury, Chem. Rev., 1993, **93**, 381-433.

37 T. Inoue , K. Kikuchi, K. Hirose, M. Iiono and T. Nagano, Chem. Biol., 2001, **8**, 9-15.

38 R. Bonnett and G. Martinez, Tetrahedron, 2001, **57**, 9513-9547.

39 B.P. Cho, T. Yang, L.R. Blankenship, J.D. Moody, M. Churchwell, F.A. Bebland and S.J. Culp, Chem. Res. Toxicol., 2003, **16**, 285-294.

40 K. Yu, S. Yang, C. Liu, H. Chen, H. Li, C. Sun and S.A. Boyd, Environ. Sci. Technol., 2012, **46**, 7318−7326.

41 W.L.W. Lee, J.S. Lin, J.L. Chang, J.Y. Chen, M.C. Cheng and C.C. Chen, J. Mol. Catal. A: Chem., 2012, **361–362**, 80–90**.**

42 F. Chen, P. Fang, Y. Gao, Z. Liu, Y. Liu and Y. Dai**,** Chem. Eng. J., 2012, **204–206**, 107–113.

43 S. Ameen, M.S. Akhtar, M. Nazim and H.S. Shin, Mater. Lett., 2013, **96**, 228–232.

44 S.T. Huang, Y.R. Jiang, S.Y. Chou, Y.M. Dai and C.C. Chen, J. Mol. Catal. A: Chem., 2014, **391**, 105–120.

45 W.L. W. Lee, W.H. Chung, W.S. Huang, W.C. Lin, W.Y. Lin, Y.R. Jiang and C.C. Chen, J. Taiwan Inst. Chem. Eng., 2013, **44**, 660–669**.**

46 Y.H. Liao, J.X. Wang, J.S. Lin, W.H. Chung, W.Y. Lin and C.C. Chen, Catal. Today, 2011, **174**, 148-159.

47 M.N. Novokreshchenova, Y. Yukhin, B.B. Bokhonov, Chem. Sustain. Dev. 2005, **13**, 563-568.

48 J. Zhang, F. Shi, J. Lin, D. Chen, J. Gao, Z. Huang, X. Ding and C. Tang, Chem. Mater., 2008, **20**, 2937-2941.

49 W.C. Lin, W.D. Yang and S.Y. Jheng, J. Taiwan Inst. Chem. Eng., 2012, **43**, 269-274.

50 L. Manna, E.C. Scher and A.P. Alivisatos, J. Cluster Sci., 2002, **13**, 521–532.

51 W.D. Wang, F.Q. Huang and X.P. Lin, Scr. Mater., 2007, **56**, 669–672.

52 K. Ishibashi, A. Fujishima, T. Watanabe and K. Hashimoto, Electrochem. Commun. 2000, **2**, 207–210.

53 L. Ye, J. Chen, L. Tian, J. Liu, T. Peng, K. Deng and L. Zan, Appl. Catal. B: Environ., 2013, **130-131**, 1– 7.

54 S. Ge and L. Zhang, Environ. Sci. Technol., 2011, 45, 3027-3033.

55 J. Wang, Y. Yu and L. Zhang, Appl. Catal. B: Environ., 2013, **136-137**, 112–121.

56 C. Yu, C. Fan, J.C. Yu, W. Zhou and K. Yang, Mater. Res. Bul., 2011, **46**, 140–146.

57 H. Fu, C. Pan, W. Yao and Y. Zhu, J. Phys. Chem. B, 2005, **109**, 22432-22439.

58 S. Kim and W. Choi, Environ. Sci. Technol., 2002, **36**, 2019-2025.

59 S.K. Sanaa, U. Vladimir, F. Sveta, P. Inna and S. Yoel, Appl. Catal. B: Environ., 2012, **117-118**, 148-155.

60 X. Xiao, R. Hao, M. Liang, X. Zuo, J. Nan, L. Li and W. Zhang, J. Hazard. Mater., 2012, **233-234**, 122-130.

61 X. Zhu, J. Zhang and F. Chen, Appl. Catal. B: Environ., 2011, **102**, 316-322.

62 K. Yu, S. Yang, C. Liu, H. Chen, H. Li, C. Sun and S.A. Boyd, Environ. Sci. Technol., 2012, **46**, 7318–7326.

63 W.W. Lee, J.S. Lin, J.L. Chang, J.Y. Chen, M.C. Cheng and C.C. Chen, J. Mol. Catal. A: Chem., 2012, **361-362**, 80-90**.**

64 L.S. Zhang, K.H. Wong, H.Y. Yip, C. Hu, J.C. Yu, C.Y. Chan and P.K. Wong, Environ. Sci. Technol, 2010, **44**, 1392-1398.

65 M.C. Yin, Z.S. Li, J.H. Kou and Z.G. Zou, Environ. Sci. Technol, 2009, **43**, 8361-8366.

66 G. Li, K.H. Wong, X. Zhang, C. Hu, J.C. Yu, R.C.Y. Chan and P.K. Wong, Chemosphere, 2009, **76**, 1185-1191.
67 S.G. Meng, D.Z. Li, M. Sun, W.J. Li, J.X. Wang, J. Chen, X.Z. Fu and G.C. Xiao, Catal. Commun., 2011,**12**, 972-975.
68 H.J. Fan, C. Lu, W.L.W. Lee, M.R. Chiou and C.C. Chen, J. Hazard. Mater., 2011, **185**, 227-235.
69 Y. Li, H. Zhang, X. Hu, X. Zhao and M. Han, J. Phys. Chem. C, 2008, **112**, 14973-14979.
70 Y.R. Jiang, H.P. Lin, W.H. Chung, Y.M. Dai, W.Y. Lin, C.C. Chen, J. Hazard. Mater., 2015, 283, 787-805.